ACS APPLIED MATERIALS & INTERFACES

www.acsami.org

Research Article

Mixed Ionic−Electronic Conducting Hydrogels with Carboxylated Carbon Nanotubes for High Performance Wearable Thermoelectric Harvesters

Chia-Yu Lee, Yen-Ting Lin, Shao-Huan Hong, Chia-Hsin Wang, U-Ser Jeng, Shih-Huang Tung, and Cheng-Liang Liu*

Cite This: *ACS Appl. Mater. Interfaces* 2023, 15, 56072−56083

Read Online

ACCESS | Metrics & More | Article Recommendations | Supporting Information

ABSTRACT: Mixed ionic−electronic conducting (MIEC) thermoelectric (TE) materials offer higher ionic conductivity and ionic Seebeck coefficient compared to those of purely ionic-conducting TE materials. These characteristics make them suitable for direct use in thermoelectric generators (TEGs) as the charge carriers can be effectively transported from one electrode to the other via the external circuit. In the present study, MIEC hydrogels are fabricated via the chemical cross-linking of polyacrylamide (PAAM) and polydopamine (PDA) to form a double network. In addition, electrically conducting carboxylated carbon nanotubes (CNT-COOH) are dispersed evenly within the hydrogel via sonication and interaction with the PDA. Moreover, the electrical properties of the hydrogel are further improved via the in situ polymerization of polyaniline (PANI). The presence of CNT-COOH facilitates the ionic conductivity and enhances the ionic Seebeck coefficient via ionic−electronic interactions between sodium ions and carboxyl groups on CNT-COOH, which can be observed in X-ray photoelectron spectroscopy results, thereby promoting the charge transport properties. As a result, the optimum device exhibits a remarkable ionic conductivity of 175.3 mS cm^{-1} and a high ionic Seebeck coefficient of 18.6 mV K^{-1}, giving an ionic power factor (PF_i) of 6.06 mW m^{-1} K^{-2} with a correspondingly impressive ionic figure of merit (ZT_i) of 2.65. These values represent significant achievements within the field of gel-state organic TE materials. Finally, a wearable module is fabricated by embedding the PAAM/PDA/CNT-COOH/PANI hydrogel into a poly(dimethylsiloxane) mold. This configuration yields a high power density of 171.4 mW m^{-2}, thus highlighting the considerable potential for manufacturing TEGs for wearable devices capable of harnessing waste heat.

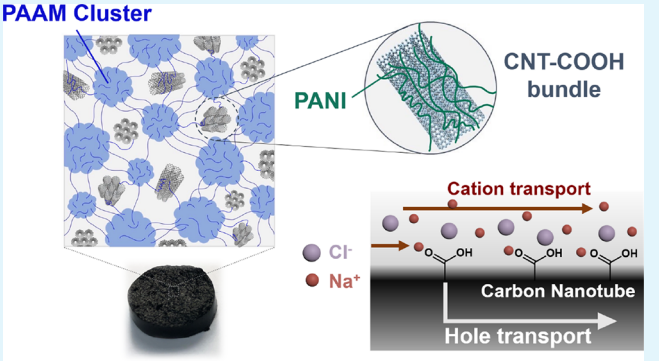

KEYWORDS: *thermoelectric, mixed ionic/electronic conductors, hydrogel, wearable device, carbon nanotubes*

INTRODUCTION

As the demand for sustainable energy solutions has increased, thermoelectric (TE) materials have emerged as a promising technology for capturing waste heat and converting it into electricity.[1−4] In this context, organic TE materials offer several advantages over their inorganic counterparts, including cost-effectiveness, flexibility, lightweight, and tunability for specific requirements.[5−12] The efficiency of TE materials is commonly assessed using the figure of merit (ZT), which is defined in eq 1:

$$ZT = S^2\sigma T/\kappa \quad (1)$$

where σ is the electrical conductivity, S is the Seebeck coefficient, κ is the thermal conductivity, and T is the absolute temperature. However, because the low thermal conductivities of organic TE materials tend to distort the ZT value, the power factor (PF, given by the product of S^2 and σ) is the most frequently used metric for evaluating the performance of organic TE materials.[13−16]

The field of TE materials has witnessed extensive research efforts in recent years, focusing on conventional materials with electrical conductors such as inorganic semiconductors,[17,18] nanocarbon materials,[19−22] and conjugated polymers.[23−25] However, despite their impressive electrical conductivities, these materials often exhibit limitations in their Seebeck coefficients. By contrast, there has been a notable surge of interest in gel-based ionically conducting TE materials due to

Received: July 9, 2023
Revised: October 28, 2023
Accepted: October 31, 2023
Published: November 20, 2023

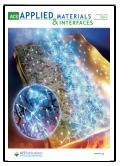

https://doi.org/10.1021/acsami.3c09934
ACS Appl. Mater. Interfaces 2023, 15, 56072−56083

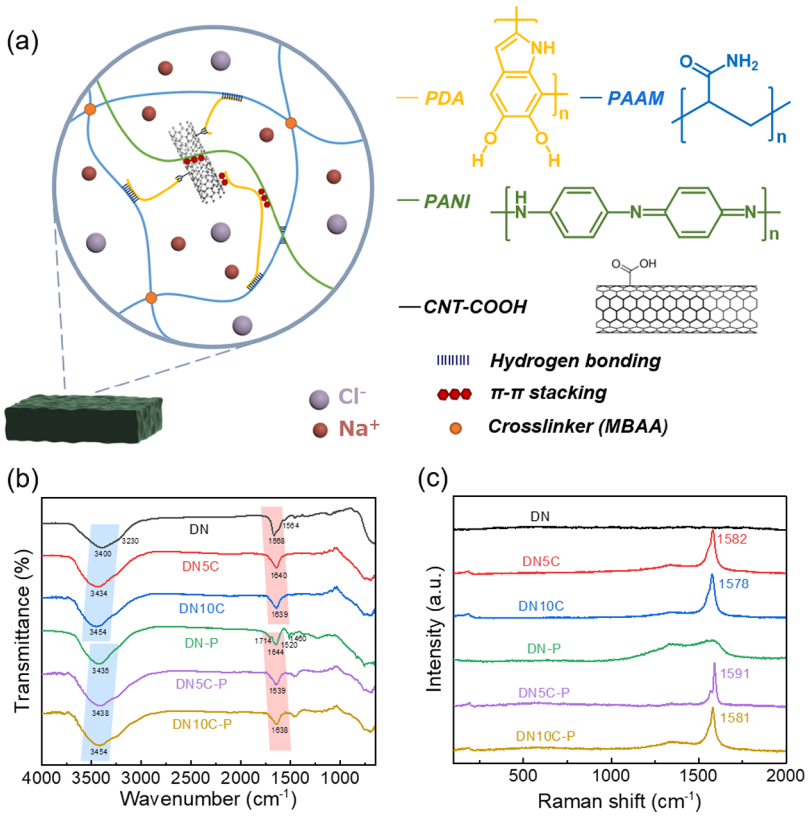

Figure 1. (a) Structure of the PDA−CNT−PAAM−PANI hydrogel and the chemical structure of PDA, PAAM, PANI, and CNT-COOH. (b) FTIR and (c) Raman spectra of the MIEC hydrogel samples.

their remarkably high ionic Seebeck coefficients (S_i), defined in eq 2:[26−31]

$$S_i = -\partial V/\partial T = -\Delta V/\Delta T = -(V_h - V_c)/(T_h - T_c) \quad (2)$$

where ΔV and ΔT are the voltage and temperature differences between the hot (V_h and T_h) and cold (V_c and T_c) sides, respectively. For instance, Zhao et al. introduced a polymeric electrolyte based on poly(ethylene oxide) (PEO) treated with sodium hydroxide (NaOH), which offers an extraordinarily high S_i of up to 11.1 mV K^{-1}.[32] This value is 2−3 orders of magnitude higher than that observed in conventional electrically conductive TE materials. The superior Seebeck coefficients of ionic TE materials can be attributed to the Soret effect, which arises from the disparate diffusivities of cations and anions, thus leading to an increase in ΔV. Nevertheless, the ionically conducting TE materials continue to face certain limitations, including low ionic conductivities (σ_i) and the difficulty in effectively transporting ions to the external electrical circuit.

To address the above-mentioned issues, mixed ionic−electronic conducting (MIEC) TE materials have emerged as a promising approach to enhancing the overall performance by establishing ionic−electronic coupling.[33−35] The pioneering work by Ail et al. introduced the use of poly(3,4-ethylenedioxythiophene):polystyrenesulfonate (PEDOT:PSS) as an MIEC TE material.[36] By subjecting the film to an ΔT of 1 °C, they achieved a time-dependent open-circuit voltage (V_{oc}) of 380 μV at 100% relative humidity (RH). Similarly, Kim et al. developed n-type MIEC polymer films incorporating cupric chloride ($CuCl_2$) as ionic conductors.[37] With a $CuCl_2$ content of 40 wt %, the as-fabricated films demonstrated a significantly high negative S_i exceeding −18.2 mV K^{-1}, a PF of 1.7 mW m^{-1} K^{-2}, and a σ_i of 52.6 mS cm^{-1} at 80% RH. Notably, the σ_i values of these films surpass the average value for pure ionic conducting TE materials, which typically stands at around 10 mS cm^{-1}. However, the fabrication of MIEC TE materials often involves the use of substrates, which can present challenges in the development of TE devices, particularly due to the interface between the TE layer and the substrate. By contrast, hydrogels possess advantages such as favorable mechanical properties and high water contents, which enable efficient ion migration. Therefore, the use of hydrogels as substrate-free platforms has become highly desirable and offers a pathway for exploring the distinctive properties and potential applications of MIEC TE materials, thus providing valuable insights for the advancement of efficient TE devices.

In the present study, MIEC hydrogels are fabricated by constructing a double network (DN) structure composed of polyacrylamide (PAAM) and polydopamine (PDA). In addition, the incorporation of functional elements, including carboxylated carbon nanotubes (CNT-COOH) and in situ polymerized polyaniline (PANI), along with sodium chloride (NaCl) as the ionic conductor, is aimed at enhancing both the ionic conductivity and Seebeck coefficient via ionic−electronic interactions and coupled transport properties. The presence of this coupling is confirmed via X-ray photoelectron spectroscopy (XPS). As a result, the optimized MIEC hydrogel exhibits a superior TE performance, with an S_i of 18.6 mV K^{-1} and a remarkably high σ_i of 175.3 mS cm^{-1}, giving an ionic PF of 6.06 mW m^{-1} K^{-2} and an ionic ZT value of 2.65. Additionally, a thermoelectric generator (TEG) is constructed by embedding the hydrogel into a poly(dimethylsiloxane) (PDMS) mold. The as-fabricated TEG exhibits a high power density of

https://doi.org/10.1021/acsami.3c09934
ACS Appl. Mater. Interfaces 2023, 15, 56072−56083

171.4 mW m^{-2}, thereby showcasing the potential of these materials for the development of wearable devices capable of efficiently harvesting waste heat.

RESULTS AND DISCUSSION

Hydrogel Preparation. As shown schematically in Figure 1a and Figure S1 of the Supporting Information, a DN hydrogel structure was fabricated consisting of two distinct PAAM and PDA networks. The PAAM served as the primary network and was chemically cross-linked using *N*,*N*′-methylene bis(acrylamide) (MBAA), while the additional PDA network was incorporated within the PAAM network and connected to it via hydrogen bonding interactions. To impart ionic conductivity, CNT-COOH was introduced to the hydrogel structure, and its dispersion in both the PDA and PAAM was facilitated by $\pi-\pi$ stacking interactions and hydrogen bonding, respectively. Additionally, the in situ polymerization of PANI was performed on the hydrogel surface to further enhance the electrical properties. The various components and corresponding sample designations are listed in Table 1. Thus, the pristine hydrogels without the incorporation of CNT-COOH and PANI are termed the DN, the hydrogels with CNT-COOH:PAAM ratios of 5 and 10% are denoted as DN5C and DN10C, respectively, and the corresponding hydrogels that are subjected to in situ polymerization with PANI are designed as DN-P, DN5C-P, and DN10C-P, respectively. Photographic images of the as-prepared samples are provided in Figure S2.

Table 1. Compositions of All the Studied Hydrogel Samples

hydrogel	CNT-COOH/AAM (wt %)[a]	DA/AAM (wt %)[a]	ANI/AAM (wt %)[a]
DN	0	0.8	0
DN5C	5	0.8	0
DN10C	10	0.8	0
DN-P	0	0.8	23
DN5C-P	5	0.8	23
DN10C-P	10	0.8	23

[a]Relative composition.

Structural Characterization. The structural characterization of the DN hydrogel was performed by using Fourier transform infrared (FTIR) and Raman spectroscopies. The FTIR spectra of the various samples are presented in Figure 1b. Here, the FTIR spectrum of DN exhibits broad and intense IR peaks at approximately 3400 and 3230 cm^{-1}, corresponding to the stretching vibrations of the O−H and N−H bonds, respectively. In addition, peaks are observed at 1714, 1643, and 1564 cm^{-1} due to C−H bending vibrations of the benzene ring, C═O stretching vibrations of the carboxylic acid and amide groups, and N−H bending vibrations of the amide groups, respectively.[38,39] With the addition of COOH, these peaks are retained, but a red shift is observed in the C═O stretching peak while a blue shift is observed in the O−H stretching peak. This suggests that the O−H groups of PDA receive electrons from the C═O groups of CNT-COOH, thus leading to the formation of additional hydrogen bonds and a more robust hydrogel structure.[40] Similar trends are observed after in situ polymerization, and the presence of PANI is confirmed by the characteristic peaks of the quinoid and benzoid structures at 1520 and 1460 cm^{-1}, respectively, in the FTIR spectra of the DN-P, DN5C-P, and DN10C-P samples.[41]

The Raman spectra of the various samples are listed in Figure 1c. Here, the CNT-COOH-containing samples are distinguished from the DN and DN-P samples by distinctive CNT peaks, which are characterized by the D and G bands at 1335 and 1582 cm^{-1}, respectively. The G band corresponds to the sp^2 carbon network, while the D band is associated with edges and defects in the sp^2 lattice of the pure CNTs.[42] A higher intensity ratio of the G band to the D band, termed the G/D ratio, indicates a lower presence of defects in the CNTs. Meanwhile, the Raman spectrum of the DN-P exhibits characteristic bands at 1350 and 1570 cm^{-1} due to the C−N^+ stretching of the semiquinone radicals and the C═C stretching of the quinoid ring, respectively, thereby suggesting the formation of conductive PANI.[43,44] Furthermore, the G band exhibits blue shifts from 1582 cm^{-1} for the DN5C to 1591 cm^{-1} for the PANI-containing DN5C-P and from 1578 cm^{-1} for the DN10C to 1581 cm^{-1} for the PANI-containing DN10C-P. As a result, the PANI can act as a bridge for charge carriers between each CNT-COOH group, thereby enhancing the electrical properties of the hydrogel surface.[45]

Valuable insights into the behavior of ions within the hydrogel are provided by the XPS results in Figure S3 and Figure 2. Thus, in Figure S3a,b, the XPS survey spectra of the DN and DN5C exhibit peaks at 533.5, 400.5, and 285.5 eV due to the O 1s, N 1s, and C 1s levels, respectively.[46] Furthermore, the presence of Na^+ and Cl^- ions within the hydrogel is confirmed by the XPS peaks at 1073.5 eV (Na 1s) and 210.5 eV (Cl 2p).[47] Meanwhile, the ion−electron coupling in the hydrogel is revealed by a shift in the Na 1s peak toward lower binding energy, i.e., from 1073.25 eV for the DN to 1073.05 eV for the DN5C (Figure 2a), thereby indicating an increase in

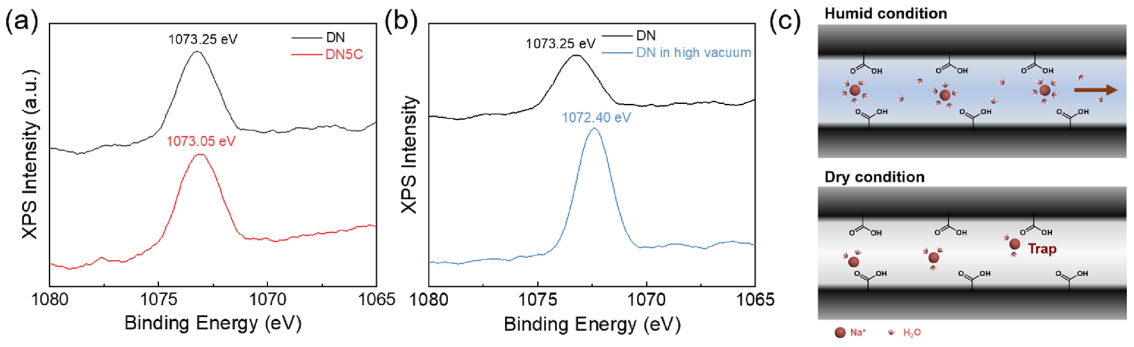

Figure 2. (a) Comparison of the XPS Na 1s peak between DN and DN5C. (b) XPS Na 1s peak of DN under humid conditions and in high vacuum. (c) Schematic representation of the ion transport model.

https://doi.org/10.1021/acsami.3c09934
ACS Appl. Mater. Interfaces 2023, 15, 56072−56083

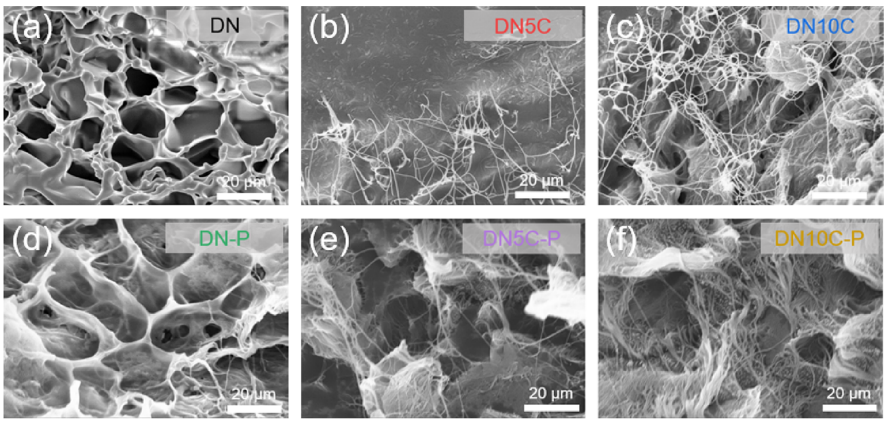

Figure 3. SEM images of (a) DN, (b), DN5C, (c) DN10C, (d) DN-P, (e) DN5C-P, and (f) DN10C-P (scale bars: 20 μm).

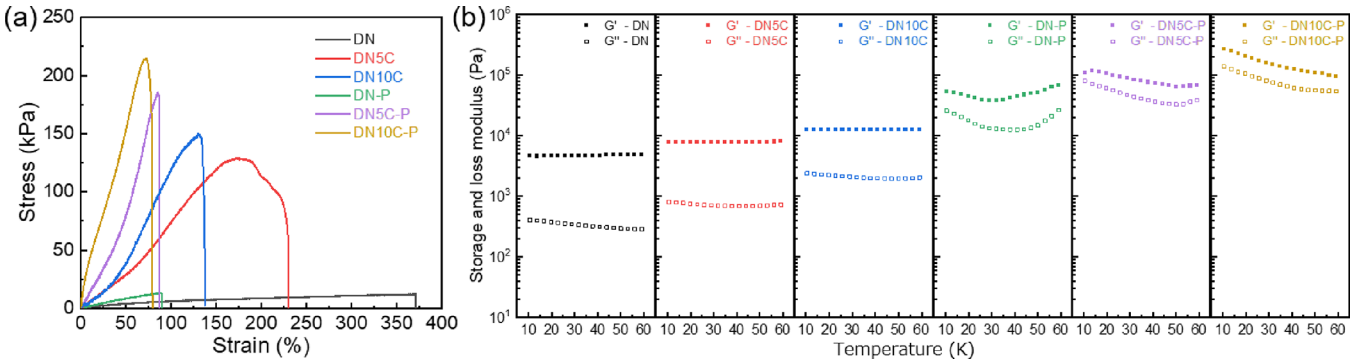

Figure 4. (a) Strain–stress curve and (b) storage modulus (G') and loss modulus (G'') of the MIEC hydrogel samples.

electron density around the Na^+ ions.[48] This, in turn, suggests that the Na^+ ions acquire electrons from the carboxyl groups of the CNT-COOH. Consequently, when the Na^+ ion is trapped by CNT-COOH during migration, the charge is effectively transferred from the Na^+ ion to CNT-COOH, thus ensuring uninterrupted charge transport. This phenomenon is discussed in greater detail in the section on thermoelectric properties. In addition, the effect of filling the chamber with water vapor to prevent the hydrogel from drying out during the XPS analysis is illustrated in Figure 2b, where the Na 1s peak of the DN observed under vacuum (0.03 mbar) exhibits a significant shift toward lower binding energy compared to that of the DN observed under humid conditions (0.5 mbar). This suggests that in the absence of moisture, almost all of the Na^+ ions form associations with the hydroxyl or carbonyl groups in the PAAM or PDA chains of the hydrogel. In the presence of moisture, however, water molecules can surround the ions to form a solvation shell, thus enabling the ions to migrate freely within the hydrogel, as shown in Figure 2c. Thus, during the diffusion process, the majority of Na^+ ions exhibit free movement with only a small fraction being trapped by the negative groups of PDA, PAAM, or CNT-COOH within the hydrogel. However, even when an ion is captured by CNT-COOH, it is still capable of transporting the charge effectively.

The morphological characteristics of the freeze-dried hydrogels are revealed by the field emission scanning electron microscopy (FE-SEM) images in Figure 3. Here, numerous micropores are observed in the DN structures of all of the hydrogel samples, thereby indicating the presence of a pathway for the facile migration of water and ions throughout the hydrogel. Furthermore, the uniform dispersion of the filamentary CNT-COOH threads in the DN10C to provide a conductive network is clearly revealed in Figure 3c. By contrast, the DN5C exhibits only a limited presence of such threads (Figure 3b), thus suggesting that the CNT-COOH molecules are not sufficiently closely packed to form an electrical transport network.[49] Meanwhile, the SEM images of DN-P, DN5C-P, and DN10C-P in Figure 3d–f reveal the presence of straight white threads traversing the micropores, thus confirming the formation of a continuous PANI layer on the hydrogel surface. This can be attributed to strong $\pi-\pi$ stacking interactions between the PANI and either the PDA or the CNT-COOH, along with hydrogen bonds between the amine groups of the PANI and the carbonyl groups of either the PAAM or the CNT-COOH. These interactions promote the uniform dispersion of PANI on the hydrogel surface. Additionally, these threads may also serve as pathways for electron transport through the hydrogel.[50] These FE-SEM observations are consistent with the results obtained from the Raman spectra, thereby further confirming the successful incorporation of CNT-COOH and PANI into the hydrogel matrix and supporting the formation of conductive pathways throughout the hydrogel matrix.

Mechanical and Rheological Properties. The mechanical properties of the hydrogels are revealed by the tensile test results in Figure 4a and Video S1. Here, all of the samples exhibit high tensile strengths of 10–200 kPa and are able to withstand strains exceeding 50%.[51] These characteristics highlight the suitability of the hydrogels for wearable device applications. Moreover, the addition of CNT-COOH significantly enhances the tensile strength of the hydrogels, which can be attributed to the strong $\pi-\pi$ stacking interactions

https://doi.org/10.1021/acsami.3c09934
ACS Appl. Mater. Interfaces 2023, 15, 56072–56083

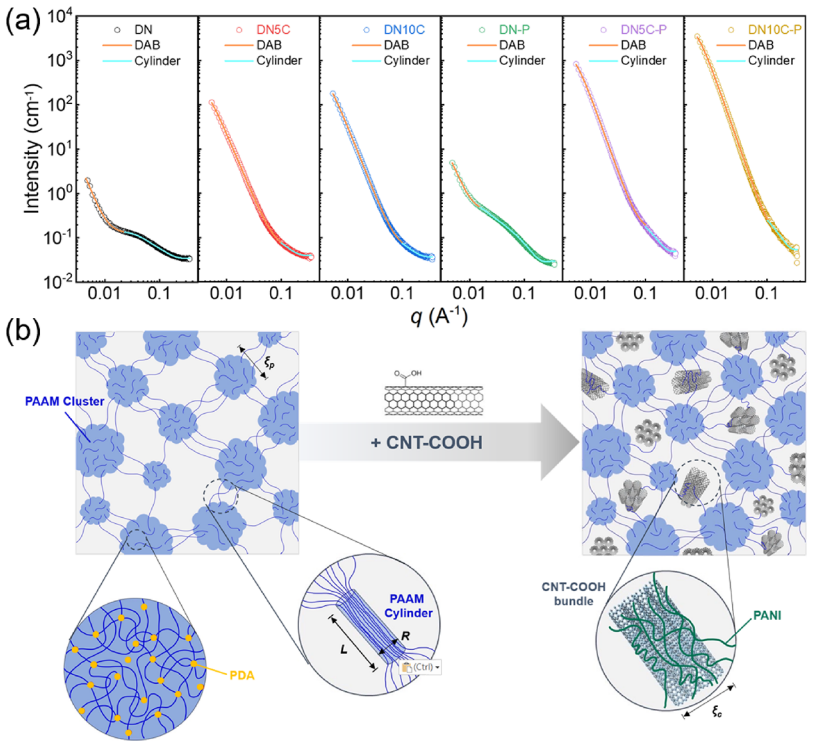

Figure 5. (a) SAXS spectra and the fit line of the MIEC hydrogel samples. (b) Schematic diagram of the hydrogel network.

between CNT-COOH and PDA, along with noncovalent interactions such as hydrogen bonding within the polymer networks. For instance, the maximum tensile stress is seen to increase from 12.3 kPa for the DN to 129.0 kPa for the DN5C, albeit with a corresponding decrease in elongation from 370 to 229%, respectively. However, the incorporation of PANI further increases the tensile strength of the hydrogel from 129.0 kPa for the DN5C to 185.6 kPa for DN5C-P while maintaining adequate stretchability with a strain of approximately 70%. This is attributed to the formation of an additional conjugated polymer network on the hydrogel surface. These findings indicate that the MIEC hydrogels possess desirable mechanical properties for applications in wearable devices.

The rheology test results in Figure 4b indicate primarily elastic behavior, where the storage modulus (G') of each hydrogel remains higher than the loss modulus (G'') throughout the temperature range of 10−60 °C. This demonstrates the ability of each hydrogel to maintain its elasticity and structural integrity.[52,53] Moreover, the magnitude of G', which reflects the resistance of the hydrogel to shearing force, increases from approximately 4.6 kPa, through 7.8 kPa, to 12.5 kPa for the DN, DN5C, and DN10C, respectively. This can be attributed to the strong $\pi-\pi$ stacking interactions between CNT-COOH and PDA, along with noncovalent interactions (e.g., hydrogen bonds) within the polymer networks. Furthermore, upon in situ polymerization with PANI, the G' values of the hydrogels are further increased to approximately 48.4, 84.6, and 514.2 kPa for the DN-P, DN5C-P, and DN10C-P hydrogels, respectively. These findings are consistent with the results obtained from the tensile testing, further highlighting the presence of an elastic network in the hydrogels and the excellent mechanical performance thereof. These properties make the hydrogels well suited for the fabrication of wearable devices and ensure their long-term use.

Small-Angle X-ray Scattering (SAXS) Measurement. The nanoscale structure of the hydrogel network is further elucidated by the SAXS profiles of the various samples in the q-range from 0.005 to 0.3 Å^{-1} in Figure 5a.[54−56] Here, the hydrogels with and without CNT-COOH exhibit very distinct profiles, especially at q < 0.1 Å^{-1}. This is due to the much stronger scattering of the large-scale CNT-COOH bundles compared to the other polymer chains so that the low-q scattering intensities of the CNT-COOH-containing hydrogels are mainly contributed by the CNT-COOH.[57,58] Therefore, the scattering data of the hydrogels with CNT-COOH are discussed separately from those without CNT-COOH in the remainder of this section. Thus, to highlight the characteristic lengths of the multidimensional structures in the various hydrogels, the scattering data are analyzed in the following two q regimes: (i) $q \sim 0.02$ Å^{-1} for the DN and DN-P and (ii) $q \sim 0.1$ Å^{-1} for the DN5C, DN10C, DN5C-P, and DN10C-P.

Because the structures of the PAAM and PDA networks can be conceptualized as joint cylinders, the scattering profiles in the high-q regime were fitted using the cylinder model described in eq 3:[59]

$$P(q) = \frac{\text{scale}}{V}\int_0^{\pi/2} F^2_{(q,\alpha)}\sin\alpha d\alpha + \text{background} \quad (3)$$

where the function $F_{(q,\alpha)}$ represents the scattering characteristics of a cylinder with radius R and length L at an angle α relative to the axis of the cylinder ($\vec{q}$). The volume (V) of the cylinder is given by $\pi R^2 L$. The scale represents the scale factor or volume fraction of cylinders. In the low-q range, the scattering profiles were analyzed using the Debye−Anderson−Brumberger (DAB) model described in eq 4:[60]

https://doi.org/10.1021/acsami.3c09934
ACS Appl. Mater. Interfaces 2023, 15, 56072−56083

$$I(q) = 8\pi\varphi(1-\varphi)\Delta\rho^2 \cdot \frac{\xi^3}{(1+(q\xi)^2)^2} + \text{background} \quad (4)$$

where q is the scattering vector, ξ is the correlation length, $\Delta\rho$ is the difference between the scattering length densities of the two phases, ϕ is the volume fraction, and the background is a fitting parameter. Thus, the DAB model determines the scattering from a two-phase system that is randomly dispersed and has distinct interfaces separated by an average distance of ξ. For the DN and DN-P, ξ represents the sizes of the large clusters of PAAM and other polymers and is designated as ξ_p; for the DN5C, DN10C, DN5C-P, and DN10C-P, however, ξ represents the sizes of the bundles of CNT-COOH and is designated as ξ_c. The values of the fitting parameters are summarized in Table 2.

Table 2. Calculated Correlation Length and Fractal Factor of All the Samples

samples	ξ_p (Å)	ξ_c (Å)	R	L
DN	358.35		13.60	93.7
DN5C		285.73	12.60	1418.7
DN10C		285.57	11.96	1552.3
DN-P	312.22		15.23	259.8
DN5C-P		214.95	11.64	593.1
DN10C-P		205.77	11.30	1079.2

Based on the fitting results, the schematic structures of the hydrogel networks are shown in Figure 5b. For the DN hydrogel, the hydrophilic amino groups and hydrophobic backbone enable the PAAM chains to assemble into cylindrical sheaves, with radii (R) of about 13.60 Å, that serve as the strands between the cross-linking points of the network. The PAAM chains further aggregate into large clusters (ξ_p = 358 Å) in the presence of PDA, which has an abundance of hydroxyl groups that attract the amino and carbonyl groups of the PAAM chains. Upon in situ polymerization with PANI, however, the radius of each cylinder in the DN-P increases to 15.23 Å, while the ξ_p value (size) of each cluster decreases to approximately 312 Å. The increased radius can be attributed to interactions between the amino groups of PANI and the carbonyl groups of PAAM, which allow PANI to bond to the PAAM sheaves. Meanwhile, the decrease in ξ_p can be attributed to the presence of $\pi-\pi$ interactions between the PANI and PDA, along with the interactions between the amino groups of PANI and the hydroxyl groups of PDA, which result in the formation of large clusters.

With the addition of CNT-COOH, the high-q fitting reveals that the radii of the cylinders decrease to 11−13 Å, which is possible because the scattering in this regime is partly contributed to by the isolated CNT-COOH with a small radius (about 10 Å). It is also possible that CNT-COOH may interfere with the assembly of the PAAM chains. The bundle size (ξ_c) of CNT-COOH extracted from the low-q regime is approximately 286 Å in both the DN5C and DN10C. Upon in situ polymerization of PANI, however, the strong $\pi-\pi$ interactions between the PANI and CNT-COOH facilitate the attachment of PANI onto the CNT-COOH surfaces, thus resulting in some disruption of the bundles. This causes the bundle sizes to decrease to 214.95 and 205.77 Å for DN5C-P and DN10C-P, respectively. This reduction in the bundle size can also be interpreted as an increase in the dispersibility of CNT-COOH within the system. These findings are in agreement with the above Raman results and provide additional evidence of the interactions between CNT-COOH and PANI. Consequently, PANI is likely to facilitate the transport of electrons between CNT-COOH chains.

The SAXS measurements in Figure S4 demonstrate the stability of the hydrogel network in various temperature regimes. There, the slopes of the scattering profiles remain relatively stable in both the low-q and high-q fittings for DN5C and DN5C-P, thus suggesting that the hydrogel network is not significantly affected by thermal fluctuations. This observation is consistent with the above-mentioned rheology test results,

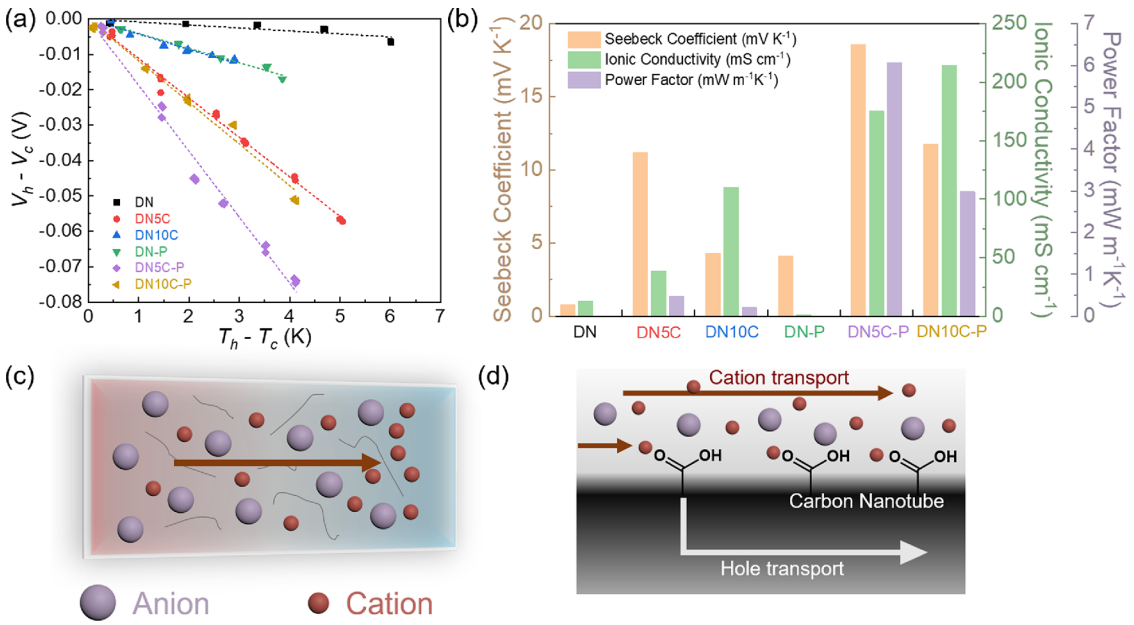

Figure 6. (a) ΔV versus ΔT curves and (b) Seebeck coefficient, ionic conductivity, and power factor of the MIEC hydrogel samples. The mechanism of (c) ionic accumulation and (d) ionic−electronic conducting.

https://doi.org/10.1021/acsami.3c09934
ACS Appl. Mater. Interfaces 2023, 15, 56072−56083

Table 3. Thermoelectric Properties of All the Studied Hydrogel Samples

samples	σ_i (mS cm^{-1})	S_i (mV K^{-1})	PF$_i$ (mW m^{-1} K^{-2})	κ (W m^{-1} K^{-1})	ZT$_i$
DN	13.1	0.8	8.4×10^{-4}	0.55	4.55×10^{-4}
DN5C	38.8	11.2	0.49	0.68	2.15×10^{-1}
DN10C	110.2	4.3	0.20	0.81	7.36×10^{-2}
DN-P	1.5	4.1	2.5×10^{-3}	0.57	1.31×10^{-3}
DN5C-P	175.3	18.6	6.06	0.68	2.65
DN10C-P	214.5	11.8	2.99	0.76	1.18

further indicating that changes in the network structure can be disregarded when considering ion diffusion in the presence of a temperature gradient.

Thermoelectric Properties. The ionic Seebeck coefficient plays a crucial role in characterizing the TE features of a material as it is used to calculate the ZT value. Hence, the $\Delta V-\Delta T$ profiles of the hydrogel samples are presented in Figure 6a, and the corresponding ionic Seebeck coefficient values (obtained from the slope of the $\Delta V-\Delta T$ profile) are shown in Figure 6b. The time-dependent relationship of DN5C-P between ΔV and ΔT is shown in Figure S5. According to earlier research, the flow of ions from the hot side of a TE material to the cold side when subjected to a temperature gradient is referred to as the Soret effect.[61−63] This ion diffusion results from the difference in ion diffusivity according to the temperature and contributes to the overall TE behavior of the material. In Figure 6a, a negative ΔV is observed when a ΔT is applied, thus indicating that cations accumulate on the cold side. This can be attributed to the repulsion between the negative functional groups, such as hydroxyl or amino groups, present in the hydrogel networks. These negative functional groups prevent the migration of anions due to Coulomb repulsion while allowing relatively smaller cations to flow between the hydrogel networks.[64] Notably, the ionic Seebeck coefficient of the material increases significantly from 0.8 mV K^{-1} for the DN to 11.2 mV K^{-1} for the DN5C. This is because most of the polymer chains in the DN behave as insulators by hindering the charge transport as ions are attracted and restricted by the negative functional groups during movement, whereas the conductive CNT-COOH enables ion−electron coupling to occur when ions are restricted during movement, thereby allowing the charge transport process to continue (Figure 6c,d). It should be noted that the amount of CNT-COOH added is insufficient to form a conducting pathway by itself, but it nevertheless contributes to the movement of ions and the generation of a high ionic Seebeck coefficient. Moreover, the ionic Seebeck coefficient of DN10C (4.3 mV K^{-1}) is even lower than that of DN5C (11.2 mV K^{-1}). This is because a higher concentration of CNT-COOH leads to the formation of more electrical transport tunnels, as observed in the SEM images (Figure 3), thereby attracting more Na^+ ions and resulting in the accumulation of fewer ions on the cold side, thus reducing the voltage difference. After the in situ polymerization of PANI, however, the ionic Seebeck coefficient is increased from 11.2 mV K^{-1} for the DN5C to 18.6 mV K^{-1} for the DN5C-P. This can be attributed to the formation of the PANI network, which facilitates the generation of an electric double layer during Na^+ ion migration, thus causing a significant ΔV between the hot and cold sides (Figure 6c).

The ionic conductivities of the various hydrogel samples are revealed by the AC impedance spectroscopy results and the corresponding equivalent circuit diagram in Figure S6 and Table S1. In this diagram, R_s represents the system's resistance, R_i and R_e signify the ionic and electronic resistance, respectively, while C_{geo} denotes the parallel plate capacitance, and C_{int} represents the electrolyte/electrode interface capacitance. The equivalent circuit diagram is referenced from a previous study, and it manifests as two semicircles in the Nyquist plot.[65−67] The radii of these semicircles are determined by the equations $R_1 = R_iR_e/(R_i + R_e)$ at high frequencies and $R_2 = R_e$ at low frequencies. However, due to the significantly lower ionic resistance in comparison to electronic resistance, only a very small semicircle is observed at high frequencies, contrasting with the larger semicircle at low frequencies. Furthermore, no low-frequency tail is evident since the interfacial capacitance is bypassed by the electronic current in the low-frequency range. Here, the calculated ionic conductivity is seen to increase from 13.1 mS cm^{-1} for the DN to 38.8 and 110.2 mS cm^{-1} for the DN5C and DN10C, respectively, due to the addition of CNT-COOH. This result can be attributed to the above-mentioned phenomenon of ionic−electronic coupling, in agreement with a previous study.[68] As noted above, because the CNT-COOH alone does not form a continuous pathway for electrical transport, the charge carriers are sequentially transported from the ions to the CNT-COOH to form an ionic−electronic couple, then released, and transported to a neighboring CNT-COOH to form another ionic−electronic couple, thereby accelerating the ionic conductivity. Moreover, because PANI is able to extend the electrical transport tunnel by connecting neighboring CNT-COOH chains, this effect becomes more pronounced after the in situ polymerization. For example, the ionic conductivity increases from 38.8 mS cm^{-1} for the DN5C to 175.3 mS cm^{-1} for the DN5C-P.

The role of ionic conductivity as the primary conducting mechanism is supported by the results in Figure S7 where the ions are shown to accumulate gradually on each side of both the DN5C and DN10C electrodes when a direct current is applied at potentials of ±200 and ±400 mV. This indicates that the influence of ion migration on charge transport can be disregarded and that the current value is solely contributed by the electrical conductor.[67] Furthermore, the resistance and electrical conductivity (σ_e) obtained from the $I-V$ curve (Figure S7) indicate that the electrical conductivity is approximately 10^4 times lower than the ionic conductivity. Additionally, the electrical conductivity of freeze-dried DN10C, which contains only electrical conductors, is found to be of the same order of magnitude (2.92×10^{-3} mS cm^{-1}).

The thermal conductivities of the various samples were analyzed using the transient plane source method,[69] where a sensor was sandwiched between two halves of each hydrogel, as shown schematically in Figure S8a. The results in Figure S8b indicate that the thermal conductivity (κ) increases from 0.55 W m^{-1} K^{-2} for the DN to 0.68 and 0.81 W m^{-1} K^{-2} for the DN5C and DN10C, respectively, due to the addition of CNT-

https://doi.org/10.1021/acsami.3c09934
ACS Appl. Mater. Interfaces 2023, 15, 56072−56083

Table 4. Thermoelectric Properties of DN5C-P Hydrogels Compared to Other MIEC and Ionic Conducting TE Materials

samples	type	ions	σ_i (mS cm^{-1})	S_i (mV K^{-1})	PF$_i$ (mW m^{-1} K^{-2})	κ (W m^{-1} K^{-1})	ZT$_i$	maximum stress (MPa)	ref.
DN5C-P	MIEC, p^a	NaCl	175.3	18.6	6.06	0.68	2.65	0.18	this work
PVA−PAMPS−PEDOT	MIEC, n^b	NH_4HSO_4	200	−26.0	13.6	0.44	9.1	N/A	71
PEDOT:PSS	MIEC, n^b	$CuCl_2$	52.6	−18.2	1.74	0.34	1.53	N/A	37
PEDOT:PSS:PSSH	MIEC, p^a	H^+	300	16.2	7.64	0.50	4.51	N/A	73
PEDOT-Tos/SWCNT	MIEC, p^a	TDAE-Tos	64	14	1.25	N/A	N/A	N/A	72
PVA	*i*-TE^c, p^a	NaI	51.5	42.8	9.43	0.54	5.18	N/A	64
oxidized cellulose membrane	*i*-TE^c, *p*	NaOH	20	2.4	1.15	0.48	0.63	N/A	74
PAAM/CMC	*i*-TE^c, p^a	NaCl	25	17.1	0.73	N/A	N/A	0.71	75
PVA	*i*-TE^c, p^a	HCl	18.9	38.2	2.75	N/A	N/A	N/A	70
P(MMA-co-MA)/ MXene	*i*-TE^c, n^b	[EMIM] [TFSI]	3.18	−8.8	0.025	0.19	0.05	4.57	76
agarose	*i*-TE^c, p^a	Na:DBS	13.2	41.8	2.30	N/A	N/A	N/A	77

^{a}p-Type TE materials. ^{b}n-Type TE materials. ^{c}Ionic conducting TE material.

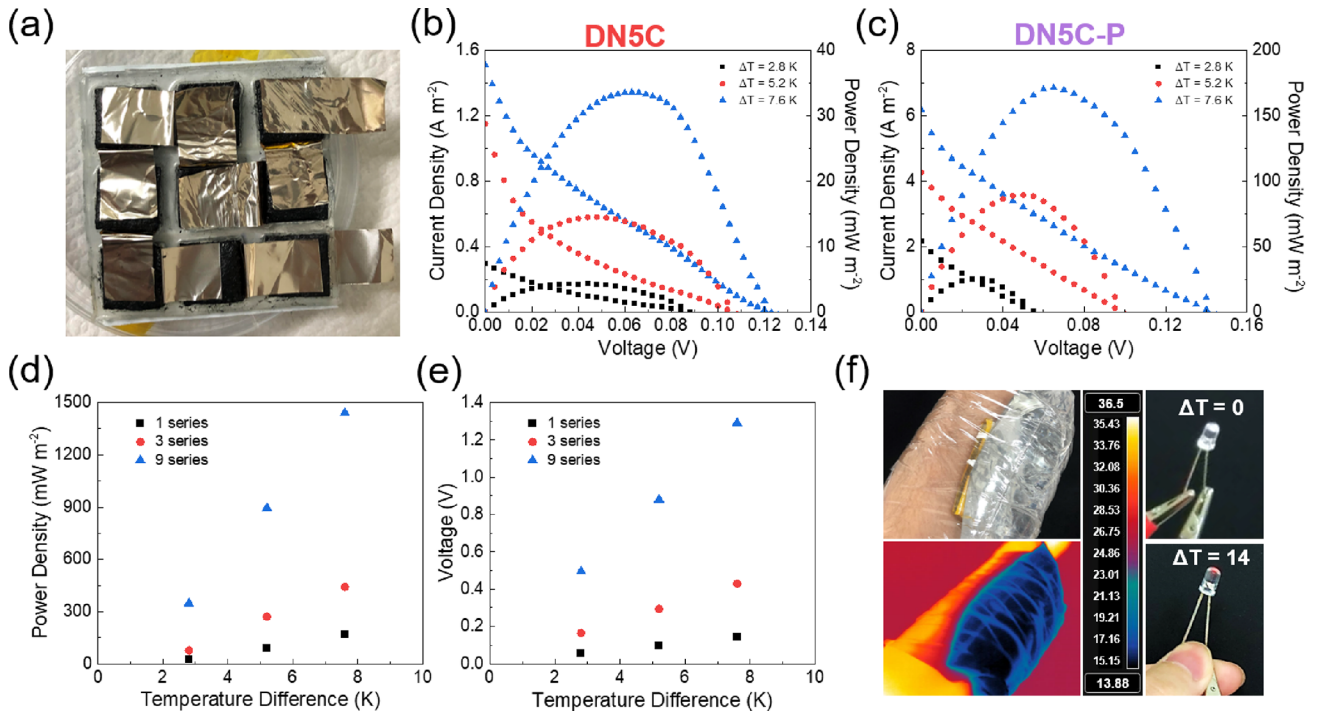

Figure 7. (a) Photograph of the 9 series of the DN5C-P connected TEG without encapsulation is presented. *I*−*V* and power density-*V* characteristics of (b) DN5C and (c) DN5C-P hydrogels. (d) Maximum power density and (e) open−circuit voltages for 1, 3, and 9 series of DN5C-P as a function of Δ*T*. (f) Practical application temperature of the TEG was captured using an infrared camera. While Δ*T* = 14, the LED light was illuminated.

COOH. However, no significant changes are observed after the addition of PANI to the hydrogels. Overall, all of the MIEC hydrogels developed herein exhibit a remarkable thermoelectric performance, with maximum ionic ZT (ZT$_i$) values of approximately 2.65 for DN5C-P, as shown in Figure 6b and Table 3. Furthermore, the performances of DN5C-P are compared with those of other MIEC and ionic conducting TE materials in Table 4.[37,64,70−77] Here, the as-prepared hydrogels exhibit mechanical properties superior to those of commonly used PEDOT:PSS-based TE materials for wearable devices. In particular, DN5C-P is seen to be highly competitive, exhibiting excellent ionic conductivity while maintaining a suitable Seebeck coefficient, thereby achieving an exceptional power factor. These results highlight the significant potential of MIEC hydrogels for practical applications in thermoelectric devices.

The three-stage charge−discharge curve of DN5C-P was meticulously analyzed to gain a deeper understanding of the charge−discharge process of the MIEC hydrogel, as illustrated in Figure S9. In the initial stage (i), with an increase in the Δ*T*, a discernible thermovoltage emerged, signifying the accumulation of Na^+ ions within the cold region. Subsequently, in stage (ii), owing to the presence of CNT-COOH and PANI, the MIEC hydrogel could release electrons to the electrodes, resulting in the discharge process with a load of 1 kΩ resistance and a voltage decrease. Finally, in stage (iii), when the Δ*T* returned to 0 K, ions returned to their equilibrium states due to concentration adjustments. In addition, an evaluation of the stability of the MIEC hydrogels was assessed by subjecting them to four continuous thermal cycling, as depicted in Figure S10. The results showcased the remarkable performance of

https://doi.org/10.1021/acsami.3c09934
ACS Appl. Mater. Interfaces 2023, 15, 56072−56083

hydrogels in response to temperature variations, thus highlighting their significant potential for utilization in thermoelectric device application.

Thermoelectric Generator. The combination of a high ZT_i and excellent mechanical properties makes the MIEC hydrogel an ideal candidate for use as a flexible thermoelectric generator (TEG). Hence, a TEG was fabricated herein using PDMS as the mold and thermal and PI tapes as the cover materials, as shown in Figure 7a. The current−voltage (I−V) and power density−voltage characteristics of the single DN5C hydrogel under temperature gradients (ΔT) of 2.8, 5.2, and 7.6 K are presented in Figure 7b. Here, the power density is seen to increase with an increase in ΔT. A sharp current drop is observed when the input voltage is first applied, which can be attributed to the presence of an electrical conductor on the surface of the hydrogel, which enables greater charge flow and disrupts the ionic−electrical couplings.[78] However, after a short period, the curve attains a more gradual slope, thereby indicating the dominance of ionic flow in the device. For comparison, the measured current−voltage (I−V) and power density−voltage characteristics of the DN are provided in Figure S11. Thus, the V_{oc} is seen to increase from 6.65 mV for the DN to 123 mV for the DN5C, while the maximum power density increases from 0.94 to 33.6 mW m^{-2} at a ΔT of 7.6 K. This can be attributed to the higher ionic Seebeck coefficient and ionic conductivity of the DN5C. Moreover, after in situ polymerization, the single DN5C-P hydrogel exhibits a significantly enhanced maximum power density of 171.4 mW m^{-2} at the same ΔT (Figure 7c). This is attributed to the presence of PANI on the hydrogel surface, which facilitates a higher current flow through the hydrogel as well as the higher ionic conductivity of the DN5C-P. In addition, the V_{oc} and power density characteristics of the DN5C-P hydrogel in configurations with 3 and 9 series connections are shown in Figure 7d,e. Here, the system exhibits a higher V_{oc} and power density of up to 0.90 V and 1439 mW m^{-2}, respectively, at a ΔT of 7.6 K in the 9 series configuration, compared to 0.43 V and 441.9 mW m^{-2}, respectively, in the 3 series configuration. These results demonstrate that a higher V_{oc} and power density can be achieved by increasing the number of series connections under a small ΔT.

Finally, to demonstrate the practical application of the TEG, nine DN5C-P hydrogels were connected in series and used to power a small LED light, as shown in Figure 7f and Video S2. In this demonstration, the TEG was attached to the skin and placed in contact with an ice bag on the other side, thereby creating a ΔT of about 14 °C. Under this condition, the TEGs successfully generated enough electrical power to turn on the LED. This demonstration showcases the potential of using MIEC hydrogels for practical electricity generation in daily life, such as in iced drink holders or under cold conditions. These TEGs can provide a convenient and sustainable power source in various scenarios where temperature gradients are present.

CONCLUSIONS

In this study, flexible mixed ionic−electronic conducting (MIEC) hydrogels with high ionic conductivities were successfully fabricated. The mechanical properties of the hydrogels were evaluated and attributed to π−π stacking interactions and noncovalent interactions within the hydrogel network. In detail, the hydrogel exhibited a maximum tensile stress of greater than 100 kPa, and a tensile strain of more than 70%. Rheology measurements and small-angle X-ray scattering (SAXS) analysis confirmed that the hydrogels maintained their elasticity and structural integrity over a temperature range of 10−60 °C. With the application of ionic−electronic coupling, the MIEC hydrogel demonstrated a remarkably high ionic conductivity of 175.3 mS cm^{-1} and a moderately high ionic Seebeck coefficient of 18.6 mV K^{-1}, thus resulting in a high ionic power factor of 6.06 mW m^{-1} K^{-2}. In addition, the hydrogel exhibited a thermal conductivity of 0.68 W m^{-1} K^{-1}, and an ionic figure of merit (ZT_i) of 2.65. Moreover, the potential practical application of the MIEC hydrogel for the effective harvesting of waste heat in a wearable device was showcased by successfully embedding it in a poly(dimethylsiloxane) (PDMS) mold to create a thermoelectric generator (TEG). The as-fabricated TEG exhibited a high power density of 171.43 mW m^{-2} under a temperature gradient of 7.6 K. These findings highlight the promise of MIEC hydrogel-based thermoelectric materials in the development of TEGs for efficient and sustainable energy technologies in the future.

EXPERIMENTAL SECTION

Materials. Dopamine (DA), hydrochloride, acrylamide (AAM), *N*,*N*′-methylenebis(acrylamide) (MBAA), and ammonium persulfate (APS) were purchased from Sigma-Aldrich. Aniline (ANI) was purchased from ACROS. Carboxylated single-walled carbon nanotubes (CNT-COOH, XFS18) with a purity of 95%, a length of 5−30 μm, and a diameter of 1−2 nm were purchased from XFNANO. All reagents and chemicals were obtained from commercial sources and used without further purification.

MIEC Hydrogel Fabrication. The MIEC hydrogels were synthesized following the procedure outlined in Figure S1. Initially, 8 mg of DA powder was dissolved in 5 mL of NaOH solution with a pH of 11. Subsequently, 0, 50, and 100 mg of CNT-COOH were added into the solution, and the mixture was sonicated for 20 min under atmospheric conditions using a Q125 sonicator (QSonica Inc.). This sonication step facilitated the formation of a PDA/CNT-COOH solution. Next, 1 g of AAM, 6 mg of MBAA, and 0.1 g of APS were added to the PDA/CNT solution in an ice bath at 4 °C. The resulting mixture was stirred for 5 min, and the AAM monomer underwent polymerization, leading to the formation of the PDA/CNT-COOH/PAAM hydrogels. The material was designated as the DN sample. To prepare two additional samples, 50 and 100 mg of CNT-COOH were added, resulting in the formation of DN5C and DN10C, respectively.

To incorporate PANI into the hydrogel structure, the DN sample was immersed in a solution containing 0.1 mol L^{-1} ANI/HCl (pH = 4) for a duration of 2 h. Following this, the hydrogel was transferred to a solution of 0.025 mol L^{-1} APS/HCl (pH = 4) and allowed to remain in this solution for 24 h. This step facilitated the in situ polymerization of the ANI monomers on the surface of the hydrogels. The resulting hydrogel sample was designed as DN-P. Similarly, two other samples were prepared by incorporating 50 and 100 mg of CNT-COOH into hydrogels, named DN5C-P and DN10C-P, respectively. To ensure the purity of the hydrogels, they were subjected to a purification process involving immersion in deionized (DI) water for 30 min and further in a 0.1 M NaCl solution for an additional 30 min.

Thermoelectric Generator Fabrication. A PDMS mold was utilized, which consisted of a 10-part base elastomer and 1-part curing agent mixture. This PDMS mold was specifically designed in a style-box shape. To achieve the desired shape, the mold was subjected to a temperature of 80 °C for 24 h. The overall dimensions of the style-box-shaped mold were 9 × 9 cm^2, with an inner vacancy measuring 1.5 × 1.5 cm^2. Nine pieces of hydrogel, measuring 1.5 × 1.5 cm^2, were precisely cut and positioned within the mold. To create the connected electrodes, a zigzag pattern was formed by folding a Ni film. Thermal tape was strategically placed on the top and bottom surfaces of the TEGs, while the sides were covered with polyimide (PI) tape. This

https://doi.org/10.1021/acsami.3c09934
ACS Appl. Mater. Interfaces 2023, 15, 56072−56083

encapsulation process effectively enclosed the entire TEG structure. It is worth noting that the thermal tape played a dual role in the fabrication process: facilitating heat conduction and ensuring proper adherence of the TEGs to the tester's skin.

Characterization and Measurement. The hydrogel samples were characterized and measured by using various techniques. Fourier transform infrared (FTIR) spectroscopy was conducted by a PerkinElmer Spectrum Two FT-IR L16000 instrument. Raman spectroscopy was performed using a Jobin Yvon LabRAM HR800 UV equipped with a 532 nm laser. The mechanical properties of hydrogel samples were assessed by using a SHIMADZU EZ Test universal testing machine. Dumbbell-shaped samples with dimensions of 5 mm width, 15 mm length, and approximately 1 mm thickness were prepared and stretched at a tension speed of 5 mm min^{-1}. Rheological characterization was conducted by using a TA Instruments HR−2 system (stress control) rheometer. The samples were subjected to an oscillation strain of 10%, frequency of 1 Hz, and a heating rate of 3 °C min^{-1}, ranging from 10 to 60 °C. Freeze-dried hydrogels were examined for the morphologies using a Hitachi S-4800 field emission scanning electron microscope (FE-SEM). Small-angle X-ray scattering (SAXS) and X-ray photoelectron spectroscopy (XPS) measurements were performed at the National Synchrotron Radiation Research Center (NSRRC) of Taiwan, utilizing Beamline TLS 23A1 and 24A1, respectively, and the measurements focused on a small portion of the hydrogel surface. The XPS analysis chamber maintained a pressure of approximately 0.05 mbar to ensure the presence of water vapor during the measurement. Thermal conductivity measurement was conducted using a Hot Disc TPS 2500S thermal constant analyzer with the standard module, employing the transient plane source (TPS) method. AC impedance spectroscopies were performed using a Biologic SP-50e electrochemical workstation with platinum (Pt) as the electrode employing a two-probe technique. The ionic conductivity (σ_i) of the hydrogel sample was calculated using the following equation:

$$\sigma_i = \frac{l}{A \times R} \tag{5}$$

where A is the cross-sectional area (about 0.7 × 0.7 cm^2) and l is the thickness (about 0.3 cm) of the sample. The thermoelectric properties of samples were measured by using a custom-built measurement system under high moisture conditions of approximately 80% RH. The temperature gradient was controlled by using a water-cooling system applied to both the hot and cold sides. Temperature was monitored by attaching K-type thermocouples attached to the sample surfaces, and voltage and current were measured by a Keithley 2182A nanovoltmeter and a Keithley 2400A, respectively, across the two Pt electrodes on the sample.

■ ASSOCIATED CONTENT

Supporting Information

The Supporting Information is available free of charge at https://pubs.acs.org/doi/10.1021/acsami.3c09934.

Further details of the preparation process and photographs of hydrogels, XPS survey spectra, the SAXS spectra under different temperatures, time-dependent relationship between the ΔV and ΔT, Nyquist plot, DC measurement, thermal conductivities, charge−discharge curve and stability test of DN5C-P, and power density of DN (PDF)

Video S1: Demonstration of the mechanical test (MOV)

Video S2: LED powered by the thermoelectric generator (MOV)

■ AUTHOR INFORMATION

Corresponding Author

Cheng-Liang Liu − *Department of Materials Science and Engineering and Advanced Research Center for Green Materials Science and Technology, National Taiwan University, Taipei 10617, Taiwan;* orcid.org/0000-0002-8778-5386; Email: liucl@ntu.edu.tw

Authors

Chia-Yu Lee − *Department of Materials Science and Engineering, National Taiwan University, Taipei 10617, Taiwan*

Yen-Ting Lin − *Department of Materials Science and Engineering, National Taiwan University, Taipei 10617, Taiwan*

Shao-Huan Hong − *Department of Chemical and Materials Engineering, National Central University, Taoyuan 32001, Taiwan*

Chia-Hsin Wang − *National Synchrotron Radiation Research Center, Hsinchu 30076, Taiwan*

U-Ser Jeng − *National Synchrotron Radiation Research Center, Hsinchu 30076, Taiwan;* orcid.org/0000-0002-2247-5061

Shih-Huang Tung − *Institute of Polymer Science and Engineering, National Taiwan University, Taipei 10617, Taiwan;* orcid.org/0000-0002-6787-4955

Complete contact information is available at: https://pubs.acs.org/10.1021/acsami.3c09934

Notes

The authors declare no competing financial interest.

■ ACKNOWLEDGMENTS

The authors acknowledge the financial support from the 2030 Cross-Generation Young Scholars Program by the National Science and Technology Council (NSTC) in Taiwan under grants 111-2628-E-002-014 and 112-2628-E-002-013 and Academic Research-Career Development Project (Sprout Research Projects) by National Taiwan University (NTU112L7856). This work was also financially supported by the "Advanced Research Center for Green Materials Science and Technology" from The Featured Area Research Center Program within the framework of the Higher Education Sprout Project by the Ministry of Education (112L9006). The authors thank Beamline TLS 23A1 and 24A1 from the National Synchrotron Radiation Research Center (NSRRC) of Taiwan for providing beamline.

■ REFERENCES

(1) Shi, X. L.; Zou, J.; Chen, Z. G. Advanced Thermoelectric Design: From Materials and Structures to Devices. *Chem. Rev.* **2020**, *120*, 7399−7515.

(2) He, J.; Tritt, T. M. Advances in Thermoelectric Materials Research: Looking Back and Moving Forward. *Science* **2017**, *357*, No. eaak9997.

(3) Massetti, M.; Jiao, F.; Ferguson, A. J.; Zhao, D.; Wijeratne, K.; Wurger, A.; Blackburn, J. L.; Crispin, X.; Fabiano, S. Unconventional Thermoelectric Materials for Energy Harvesting and Sensing Applications. *Chem. Rev.* **2021**, *121*, 12465−12547.

(4) Chen, W.-Y.; Shi, X.-L.; Zou, J.; Chen, Z.-G. Wearable Fiber-Based Thermoelectrics from Materials to Applications. *Nano Energy* **2021**, *81*, No. 105684.

(5) Cao, T.; Shi, X.-L.; Chen, Z.-G. Advances in the Design and Assembly of Flexible Thermoelectric Device. *Prog. Mater. Sci.* **2023**, *131*, No. 101003.

(6) Zhang, Q.; Sun, Y.; Xu, W.; Zhu, D. Organic Thermoelectric Materials: Emerging Green Energy Materials Converting Heat to

Electricity Directly and Efficiently. *Adv. Funct. Mater.* **2014**, *26*, 6829−6851.
(7) Petsagkourakis, I.; Tybrandt, K.; Crispin, X.; Ohkubo, I.; Satoh, N.; Mori, T. Thermoelectric Materials and Applications for Energy Harvesting Power Generation. *Sci. Technol. Adv. Mater.* **2018**, *19*, 836−862.
(8) Yao, H.; Fan, Z.; Cheng, H.; Guan, X.; Wang, C.; Sun, K.; Ouyang, J. Recent Development of Thermoelectric Polymers and Composites. *Macromol. Rapid Commun.* **2018**, *39*, 1700727.
(9) Prunet, G.; Pawula, F.; Fleury, G.; Cloutet, E.; Robinson, A. J.; Hadziioannou, G.; Pakdel, A. A Review on Conductive Polymers and Their Hybrids for Flexible and Wearable Thermoelectric Applications. *Mater. Today Phys.* **2021**, *18*, No. 100402.
(10) Russ, B.; Glaudell, A.; Urban, J. J.; Chabinyc, M. L.; Segalman, R. A. Organic Thermoelectric Materials for Energy Harvesting and Temperature Control. *Nat. Rev. Mater.* **2016**, *1*, 16050.
(11) Nandihalli, N.; Liu, C.-J.; Mori, T. Polymer Based Thermoelectric Nanocomposite Materials and Devices: Fabrication and Characteristics. *Nano Energy* **2020**, *78*, No. 105186.
(12) Wang, H.; Yu, C. Organic Thermoelectrics: Materials Preparation, Performance Optimization, and Device Integration. *Joule* **2019**, *3*, 53−80.
(13) He, R.; Schierning, G.; Nielsch, K. Thermoelectric Devices: A Review of Devices, Architectures, and Contact Optimization. *Adv. Mater. Technol.* **2018**, *3*, 1700256.
(14) Shi, X.-L.; Chen, W.-Y.; Zhang, T.; Zou, J.; Chen, Z.-G. Fiber-Based Thermoelectrics for Solid, Portable, and Wearable Electronics. *Energy Environ. Sci.* **2021**, *14*, 729−764.
(15) Wu, H.; Shi, X.-l.; Duan, J.; Liu, Q.; Chen, Z.-G. Advances in Ag_2Se-Based Thermoelectrics from Materials to Applications. *Energy Environ. Sci.* **2023**, *16*, 1870−1906.
(16) Xu, S.; Shi, X.-L.; Dargusch, M.; Di, C.; Zou, J.; Chen, Z.-G. Conducting Polymer-Based Flexible Thermoelectric Materials and Devices: From Mechanisms to Applications. *Prog. Mater. Sci.* **2021**, *121*, No. 100840.
(17) Eslamian, M. Inorganic and Organic Solution-Processed Thin Film Devices. *Nano-Micro Lett.* **2017**, *9*, 3.
(18) Heremans, J. P.; Wiendlocha, B.; Chamoire, A. M. Resonant Levels in Bulk Thermoelectric Semiconductors. *Energy Environ. Sci.* **2012**, *5*, 5510−5530.
(19) Dey, A.; Bajpai, O. P.; Sikder, A. K.; Chattopadhyay, S.; Shafeeuulla Khan, M. A. Recent Advances in CNT/Graphene Based Thermoelectric Polymer Nanocomposite: A Proficient Move Towards Waste Energy Harvesting. *Renewable Sustainable Energy Rev.* **2016**, *53*, 653−671.
(20) Jang, Y.; Kim, S. M.; Spinks, G. M.; Kim, S. J. Carbon Nanotube Yarn for Fiber-Shaped Electrical Sensors, Actuators, and Energy Storage for Smart Systems. *Adv. Funct. Mater.* **2020**, *32*, 1902670.
(21) Wang, X.; Wang, H.; Liu, B. Carbon Nanotube-Based Organic Thermoelectric Materials for Energy Harvesting. *Polymers* **2018**, *10*, 1196.
(22) Zhang, Y.; Heo, Y. J.; Park, M.; Park, S. J. Recent Advances in Organic Thermoelectric Materials: Principle Mechanisms and Emerging Carbon-Based Green Energy Materials. *Polymers* **2019**, *11*, 167.
(23) Kim, G. H.; Shao, L.; Zhang, K.; Pipe, K. P. Engineered Doping of Organic Semiconductors for Enhanced Thermoelectric Efficiency. *Nat. Mater.* **2013**, *12*, 719−723.
(24) Scaccabarozzi, A. D.; Basu, A.; Anies, F.; Liu, J.; Zapata-Arteaga, O.; Warren, R.; Firdaus, Y.; Nugraha, M. I.; Lin, Y.; Campoy-Quiles, M.; et al. Doping Approaches for Organic Semiconductors. *Chem. Rev.* **2022**, *122*, 4420−4492.
(25) Yao, C. J.; Zhang, H. L.; Zhang, Q. Recent Progress in Thermoelectric Materials Based on Conjugated Polymers. *Polymers* **2019**, *11*, 107.
(26) Cheng, H.; Le, Q.; Liu, Z.; Qian, Q.; Zhao, Y.; Ouyang, J. Ionic Thermoelectrics: Principles, Materials and Applications. *J. Mater. Chem. C* **2022**, *10*, 433−450.
(27) Zhao, D.; Würger, A.; Crispin, X. Ionic Thermoelectric Materials and Devices. *J. Energy Chem.* **2021**, *61*, 88−103.
(28) Liu, Y.; Cui, M.; Ling, W.; Cheng, L.; Lei, H.; Li, W.; Huang, Y. Thermo-Electrochemical Cells for Heat to Electricity Conversion: from Mechanisms, Materials. *Strategies to Applications. Energy Environ. Sci.* **2022**, *15*, 3670−3687.
(29) Pai, Y. H.; Tang, J.; Zhao, Y.; Liang, Z. Ionic Organic Thermoelectrics with Impressively High Thermopower for Sensitive Heat Harvesting Scenarios. *Adv. Energy Mater.* **2022**, *13*, 2202507.
(30) Sun, S.; Li, M.; Shi, X.; Chen, Z. Advances in Ionic Thermoelectrics: From Materials to Devices. *Adv. Energy Mater.* **2023**, *13*, 2203692.
(31) Wang, S.; Han, L.; Liu, H.; Dong, Y.; Wang, X. Ionic Gelatin-Based Flexible Thermoelectric Generator with Scalability for Human Body Heat Harvesting. *Energies* **2022**, *15*, 3441.
(32) Zhao, D.; Wang, H.; Khan, Z. U.; Chen, J. C.; Gabrielsson, R.; Jonsson, M. P.; Berggren, M.; Crispin, X. Ionic Thermoelectric Supercapacitors. *Energy Environ. Sci.* **2016**, *9*, 1450−1457.
(33) Paulsen, B. D.; Fabiano, S.; Rivnay, J. Mixed Ionic-Electronic Transport in Polymers. *Annu. Rev. Mater. Res.* **2021**, *51*, 73−99.
(34) Qiu, P.; Agne, M. T.; Liu, Y.; Zhu, Y.; Chen, H.; Mao, T.; Yang, J.; Zhang, W.; Haile, S. M.; Zeier, W. G.; et al. Suppression of Atom Motion and Metal Deposition in Mixed Ionic Electronic Conductors. *Nat. Commun.* **2018**, *9*, 2910.
(35) Thomas, E. M.; Nguyen, P. H.; Jones, S. D.; Chabinyc, M. L.; Segalman, R. A. Electronic, Ionic, and Mixed Conduction in Polymeric Systems. *Annu. Rev. Mater. Res.* **2021**, *51*, 1−20.
(36) Ail, U.; Jafari, M. J.; Wang, H.; Ederth, T.; Berggren, M.; Crispin, X. Thermoelectric Properties of Polymeric Mixed Conductors. *Adv. Funct. Mater.* **2016**, *26*, 6288−6296.
(37) Kim, B.; Hwang, J. U.; Kim, E. Chloride Transport in Conductive Polymer Films for an n-Type Thermoelectric Platform. *Energy Environ. Sci.* **2020**, *13*, 859−867.
(38) Zhao, Z.; Chen, H.; Zhang, H.; Ma, L.; Wang, Z. Polyacrylamide-Phytic Acid-Polydopamine Conducting Porous Hydrogel for Rapid Detection and Removal of Copper (II) Ions. *Biosens. Bioelectron.* **2017**, *91*, 306−312.
(39) Xie, Z.; Li, H.; Mi, H.-Y.; Feng, P.-Y.; Liu, Y.; Jing, X. Freezing-Tolerant, Widely Detectable and Ultra-Sensitive Composite Organohydrogel for Multiple Sensing Applications. *J. Mater. Chem. C* **2021**, *9*, 10127−10137.
(40) Hobza, P.; Havlas, Z. Blue-Shifting Hydrogen Bonds. *Chem. Rev.* **2000**, *100*, 4253−4264.
(41) Yellappa, M.; Sravan, J. S.; Sarkar, O.; Reddy, Y. V. R.; Mohan, S. V. Modified Conductive Polyaniline-Carbon Nanotube Composite Electrodes for Bioelectricity Generation and Waste Remediation. *Bioresour. Technol.* **2019**, *284*, 148−154.
(42) Zhang, J.; Zhu, A. Study on the Synthesis of PANI/CNT Nanocomposite and its Anticorrosion Mechanism in Waterborne Coatings. *Prog. Org. Coat.* **2021**, *159*, No. 106447.
(43) Qu, C.; Zhao, P.; Ren, Y.; Wu, C.; Liu, J. Increase the Surface PANI Occupancy of Electrospun PMMA/PANI Fibers: Effect of the Electrospinning Parameters on Surface Segregation. *Polymers* **2022**, *14*, 3401.
(44) Słoniewska, A.; Pałys, B. Supramolecular Polyaniline Hydrogel as a Support for Urease. *Electrochim. Acta* **2014**, *126*, 90−97.
(45) do Nascimento, G. M.; Silva, T. B.; Corio, P.; Dresselhaus, M. S. Charge-Transfer Behavior of Polyaniline Single Wall Carbon Nanotubes Nanocomposites Monitored by Resonance Raman Spectroscopy. *J. Raman Spectrosc.* **2010**, *41*, 1587−1593.
(46) Aditya, T.; Jana, J.; Pal, A.; Pal, T. One-Pot Fabrication of Perforated Graphitic Carbon Nitride Nanosheets Decorated with Copper Oxide by Controlled Ammonia and Sulfur Trioxide Release for Enhanced Catalytic Activity. *ACS Omega* **2018**, *3*, 9318−9332.
(47) Cheng, M. H.; Callahan, K. M.; Margarella, A. M.; Tobias, D. J.; Hemminger, J. C.; Bluhm, H.; Krisch, M. J. Ambient Pressure X-ray Photoelectron Spectroscopy and Molecular Dynamics Simulation Studies of Liquid/Vapor Interfaces of Aqueous NaCl, RbCl, and RbBr Solutions. *J. Phys. Chem. C* **2012**, *116*, 4545−4555.

https://doi.org/10.1021/acsami.3c09934
ACS Appl. Mater. Interfaces 2023, 15, 56072−56083

(48) Nesbitt, H. W.; Bancroft, G. M.; Henderson, G. S.; Ho, R.; Dalby, K. N.; Huang, Y.; Yan, Z. Bridging, Non-Bridging and Free (O^{2-}) Oxygen in Na_2O-SiO_2 Glasses: An X-ray Photoelectron Spectroscopic (XPS) and Nuclear Magnetic Resonance (NMR) Study. *J. Non-Cryst.* **2011**, *357*, 170−180.
(49) Yaghoubi, A.; Ramazani, A.; Ghasemzadeh, H. Synthesis of Physically Crosslinked PAM/CNT Flakes Nanocomposite Hydrogel Films via a Destructive Approach. *RSC Adv.* **2021**, *11*, 39095−39107.
(50) Wang, Q.; Yao, Q.; Chang, J.; Chen, L. Enhanced Thermoelectric Properties of CNT/PANI Composite Nanofibers by Highly Orienting the Arrangement of Polymer Chains. *J. Mater. Chem.* **2012**, *22*, 17612−17618.
(51) Souri, H.; Banerjee, H.; Jusufi, A.; Radacsi, N.; Stokes, A. A.; Park, I.; Sitti, M.; Amjadi, M. Wearable and Stretchable Strain Sensors: Materials, Sensing Mechanisms, and Applications. *Adv. Intell. Syst.* **2020**, *2*, 2000039.
(52) Chen, Q.; Cheng, B.; Wang, Z.; Sun, X.; Liu, Y.; Sun, H.; Li, J.; Chen, L.; Zhu, X.; Huang, L.; et al. Rarely Negative-Thermovoltage Cellulose Ionogel with Simultaneously Boosted Mechanical Strength and Ionic Conductivity via Ion-Molecular Engineering. *J. Mater. Chem. A* **2023**, *11*, 2145−2154.
(53) Villar-Chavero, M. M.; Dominguez, J. C.; Alonso, M. V.; Oliet, M.; Rodriguez, F. Tuning the Rheological Properties of Cellulosic Ionogels Reinforced with Chitosan: The Role of the Deacetylation Degree. *Carbohydr. Polym.* **2019**, *207*, 775−781.
(54) Ju, D.; Kim, D.; Yook, H.; Han, J. W.; Cho, K. Controlling Electrostatic Interaction in PEDOT:PSS to Overcome Thermoelectric Tradeoff Relation. *Adv. Funct. Mater.* **2019**, *29*, 1905590.
(55) Tian, T.; Yin, S.; Tu, S.; Weindl, C. L.; Wienhold, K. S.; Liang, S.; Schwartzkopf, M.; Roth, S. V.; Müller-Buschbaum, P. Morphology Transformation Pathway of Block Copolymer-Directed Cooperative Self-Assembly of ZnO Hybrid Films Monitored In Situ during Slot-Die Coating. *Adv. Funct. Mater.* **2021**, *31*, 2105644.
(56) Li, X.; Zou, R.; Liu, Z.; Mata, J.; Storer, B.; Chen, Y.; Qi, W.; Zhou, Z.; Zhang, P. Deciphering the Superior Thermoelectric Property of Post-Treatment-Free PEDOT:PSS/IL Hybrid by X-ray and Neutron Scattering Characterization. *NPJ Flexible Electron.* **2022**, *6*, 6.
(57) Gubaidullin, A. T.; Makarova, A. O.; Derkach, S. R.; Voron'ko, N. G.; Kadyirov, A. I.; Ziganshina, S. A.; Salnikov, V. V.; Zueva, O. S.; Zuev, Y. F. Modulation of Molecular Structure and Mechanical Properties of κ-Carrageenan-Gelatin Hydrogel with Multi-Walled Carbon Nanotubes. *Polymers* **2022**, *14*, 2346.
(58) Zueva, O. S.; Gubaidullin, A. T.; Makarova, A. O.; Bogdanova, L. R.; Zakharova, L. Y.; Zuev, Y. F. Structural Features of Composite Protein-Polysaccharide Hydrogel in the Presence of a Carbon Nanomaterial. *Russ. Chem. Bull.* **2020**, *69*, 581−589.
(59) Pedersen, J. S. Analysis of Small-Angle Scattering Data from Colloids and Polymer Solutions: Modeling and Least-Squares Fitting. *Adv. Colloid* **1997**, *70*, 171−210.
(60) Debye, P.; Anderson, H. R., Jr; Brumberger, H. Scattering by an Inhomogeneous Solid. II. The Correlation Function and Its Application. *J. Appl. Phys.* **1957**, *28*, 679−683.
(61) Pires, A. L.; Costa, R. S.; Pereira, C.; Pereira, A. M. An Interdigital Planar Energy Harvesting/Storage Device Based On an Ionic Solid−Gel Polymer. *ACS Appl. Electron. Mater.* **2021**, *3*, 696−703.
(62) Jiang, Q.; Sun, H.; Zhao, D.; Zhang, F.; Hu, D.; Jiao, F.; Qin, L.; Linseis, V.; Fabiano, S.; Crispin, X.; et al. High Thermoelectric Performance in n-Type Perylene Bisimide Induced by the Soret Effect. *Adv. Funct. Mater.* **2020**, *32*, 2002752.
(63) Guan, X.; Cheng, H.; Ouyang, J. Significant Enhancement in the Seebeck Coefficient and Power Factor of Thermoelectric Polymers by the Soret Effect of Polyelectrolytes. *J. Mater. Chem. A* **2018**, *6*, 19347−19352.
(64) He, Y.; Zhang, Q.; Cheng, H.; Liu, Y.; Shu, Y.; Geng, Y.; Zheng, Y.; Qin, B.; Zhou, Y.; Chen, S.; et al. Role of Ions in Hydrogels with an Ionic Seebeck Coefficient of 52.9 mV K^{-1}. *J. Phys. Chem. Lett.* **2022**, *13*, 4621−4627.
(65) Huggins, R. A. Simple Method to Determine Electronic and Ionic Components of the Conductivity in Mixed Conductors a Review. *Ionics* **2002**, *8*, 300−313.
(66) Del Olmo, R.; Forsyth, M.; Casado, N. Mixed Ionic-Electronic Conductors Based on Polymer Composites. In *Advances in Nanocomposite Materials for Environmental and Energy Harvesting Applications*, Shalan, A. E., Hamdy Makhlouf, A. S., Lanceros-Méndez, S., Eds.; Springer International Publishing, 2022; pp 493−532 DOI: 10.1007/978-3-030-94319-6_17.
(67) Wang, S.; Yan, M.; Li, Y.; Vinado, C.; Yang, J. Separating Electronic and Ionic Conductivity in Mix-Conducting Layered Lithium Transition-Metal Oxides. *J. Power Sources* **2018**, *393*, 75−82.
(68) Cao, L.; Wu, H.; Mu, Z.; He, X.; Wang, C.; Li, J.; Li, Y.; Xu, M.; Jiang, Z. Phosphorylated Graphene Monoliths with High Mixed Proton/Electron Conductivity. *J. Mater. Chem. A* **2018**, *6*, 8499−8506.
(69) Cheng, H.; Yue, S.; Le, Q.; Qian, Q.; Ouyang, J. A Mixed Ion-Electron Conducting Carbon Nanotube Ionogel to Efficiently Harvest Heat from both a Temperature Gradient and Temperature Fluctuation. *J. Mater. Chem. A* **2021**, *9*, 13588−13596.
(70) Chen, Q.; Chen, B.; Xiao, S.; Feng, J.; Yang, J.; Yue, Q.; Zhang, X.; Wang, T. Giant Thermopower of Hydrogen Ion Enhanced by a Strong Hydrogen Bond System. *ACS Appl. Mater. Interfaces* **2022**, *14*, 19304−19314.
(71) Cho, C.; Kim, B.; Park, S.; Kim, E. Bisulfate Transport in Hydrogels for Self-Healable and Transparent Thermoelectric Harvesting Films. *Energy Environ. Sci.* **2022**, *15*, 2049−2060.
(72) Choi, K.; Kim, S. L.; Yi, S. I.; Hsu, J. H.; Yu, C. Promoting Dual Electronic and Ionic Transport in PEDOT by Embedding Carbon Nanotubes for Large Thermoelectric Responses. *ACS Appl. Mater. Interfaces* **2018**, *10*, 23891−23899.
(73) Kim, B.; Na, J.; Lim, H.; Kim, Y.; Kim, J.; Kim, E. Robust High Thermoelectric Harvesting Under a Self-Humidifying Bilayer of Metal Organic Framework and Hydrogel Layer. *Adv. Funct. Mater.* **2019**, *29*, 1807549.
(74) Li, T.; Zhang, X.; Lacey, S. D.; Mi, R.; Zhao, X.; Jiang, F.; Song, J.; Liu, Z.; Chen, G.; Dai, J.; et al. Cellulose Ionic Conductors with High Differential Thermal Voltage for Low-Grade Heat Harvesting. *Nat. Mater.* **2019**, *18*, 608−613.
(75) Yang, X.; Tian, Y.; Wu, B.; Jia, W.; Hou, C.; Zhang, Q.; Li, Y.; Wang, H. High-Performance Ionic Thermoelectric Supercapacitor for Integrated Energy Conversion-Storage. *Energy Environ. Mater.* **2022**, *5*, 954−961.
(76) Zhao, W.; Lei, Z.; Wu, P. Mechanically Adaptative and Environmentally Stable Ionogels for Energy Harvest. *Adv. Sci.* **2023**, *10*, No. e2300253.
(77) Li, Q.; Yu, D.; Wang, S.; Zhang, X.; Li, Y.; Feng, S. P.; Liu, W. High Thermopower of Agarose-Based Ionic Thermoelectric Gel Through Micellization Effect Decoupling the Cation/Anion Thermodiffusion. *Adv. Funct. Mater.* **2023**, 2305835,
(78) Kim, S. J.; Lee, H. E.; Choi, H.; Kim, Y.; We, J. H.; Shin, J. S.; Lee, K. J.; Cho, B. J. High-Performance Flexible Thermoelectric Power Generator Using Laser Multiscanning Lift-Off Process. *ACS Nano* **2016**, *10*, 10851−10857.